Continuous Faraday measurement of spin precession without light shifts

M. Jasperse, M. J. Kewming,[*] S. N. Fischer, P. Pakkiam,[†] R. P. Anderson, and L. D. Turner[‡]
School of Physics & Astronomy, Monash University, Victoria 3800, Australia
(Received 31 May 2017; revised manuscript received 21 July 2017; published 1 December 2017)

We describe a dispersive Faraday optical probe of atomic spin which performs a weak measurement of spin projection of a quantum gas continuously for more than one second. To date, focusing bright far-off-resonance probes onto quantum gases has proved invasive due to strong scalar and vector light shifts exerting dipole and Stern-Gerlach forces. We show that tuning the probe near the magic-zero wavelength at 790 nm between the fine-structure doublet of ^{87}Rb cancels the scalar light shift, and careful control of polarization eliminates the vector light shift. Faraday rotations due to each fine-structure line reinforce at this wavelength, enhancing the signal-to-noise ratio for a fixed rate of probe-induced decoherence. Using this minimally invasive spin probe, we perform microscale atomic magnetometry at high temporal resolution. Spectrogram analysis of the Larmor precession signal of a single spinor Bose-Einstein condensate measures a time-varying magnetic field strength with 1 μG accuracy every 5 ms; or, equivalently, makes more than 200 successive measurements each at 10 pT/$\sqrt{\text{Hz}}$ sensitivity.

DOI: 10.1103/PhysRevA.96.063402

I. INTRODUCTION

Dispersive probes of quantum systems deliver temporally rich data, expose fluctuating and critical processes, maximally exploit long coherence times, and enable feedback control. The Faraday light-matter interface couples atomic spin via the off-resonant vector electric dipole interaction to optical polarization, which is readily measured at the quantum limit. Faraday measurements have opened new perspectives in quantum metrology [1], quantum information [2], nonlinear mean-field [3] and many-body [4] systems, and have potential for probing strongly correlated systems [5]. The Faraday interface has been applied to progressively colder systems: magneto-optical traps [6], dark- [7] and bright-optical dipole traps [4,8–12], and Bose-Einstein condensates (BEC) [3,13]. However, the classical backaction of the Faraday probe perturbs atomic motional and spin degrees of freedom, limiting and confounding measurements of emergent phenomena or weak external fields at ultracold temperatures. Here we explore theoretically and experimentally a magic-wavelength Faraday probe which minimizes classical backaction, and so enables continuous measurements of a coherent spinor quantum gas beyond one second.

A. The Faraday light-matter interface

The resonant Faraday effect is the enhanced rotation of light polarization by an atomic vapor in the wings of absorption lines, first observed in 1898 [14]. As a spectroscopic tool, the effect has been exploited for ultranarrow optical filters [15,16], ultrasensitive spectroscopy [17], laser stabilization [18], and optical frequency standards [19]. Resonant Faraday probing of spins undergoing Larmor precession results in the polarization angle of transmitted light oscillating at the Larmor frequency. Such polarization modulation is readily photodetected with a balanced polarimeter, and given knowledge of the gyromagnetic ratio yields calibration-free "optical magnetometry," which is widely implemented in warm atomic vapors [20]. Faraday probes enable quantum state tomography of atomic gases, measuring a single projection of the spin in the laboratory frame while the spin state is evolved by applied radio-frequency and microwave fields [21,22], or by spin-mixing interactions in a degenerate spinor gas [3].

When the coupling between the light polarization and spin polarization is strong, the quantum backaction of the light rotating the spins becomes important, and the Faraday interaction is considered a "quantum light-matter interface" [23], rather than an optical probe of an unperturbed atomic sample. Used with warm atomic vapors, this "Faraday interface" has squeezed spins [24], squeezed light [25], entangled states of collective atomic ensembles [26], encoded light into quantum memories [27], and teleported states of light to atoms [28]. Applied to ultracold (but not degenerate) atoms [8], the Faraday interface has created macroscopic singlet states [4], squeezed two spin projections simultaneously [12], cooled by feedback [10] and made macroscopic quantum nondemolition measurements [11].

B. Choice of detuning

The parameters of the Faraday interface itself—in both strong- and weak-coupling regimes—have been studied, including the optimal spatial mode and its effects on quantum noise [29] and backaction [30], the temporal mode for pulsed probes [31], and the effect of polarization on tensor light shifts [32]. The effect of probe detuning Δ, however, has only been studied in terms of the off-resonant photon-scattering rate, i.e., the incoherent component of the backaction of the probe on the atoms. In the case of a probe far-detuned from an isolated spectral line, the Faraday rotation angle is dispersive and falls off as $1/\Delta$, yielding a polarimeter signal proportional to I_0/Δ for probe intensity I_0. Because the photon quantum noise of this probe is proportional to $\sqrt{I_0}$, the photon-limited signal-to-noise ratio (SNR) for a Faraday measurement scales as $\sqrt{I_0}/\Delta$ or, equivalently, as $\sqrt{\gamma_s}$, where γ_s is the off-resonant photon-scattering rate [33]. This two-level Faraday measurement model has been extended to a more realistic atomic structure, including all hyperfine

[*]Present address: School of Mathematics and Physics, University of Queensland, St Lucia Qld 4072, Australia.
[†]Present address: School of Physics, University of New South Wales, Sydney NSW 2052, Australia.
[‡]lincoln.turner@monash.edu

lines of a *single* fine-structure transition [34]. These models conclude that the Faraday SNR depends strictly on scattering rate, with detuning a free parameter; e.g., one can choose a low-intensity probe tuned close to resonance or a brighter beam at larger detuning.

The experimenter is soon caught in a dilemma. A practical choice is to use the brightest possible beam, to overwhelm the technical noise in the photodetector, and sufficiently detuned to reduce the scattering rate to the maximum permissible level. The *coherent* backaction of this bright, off-resonant beam includes a scalar light shift of the atomic eigenstates, which scales as $I_0/\Delta \propto \gamma_s \Delta$, and for a spatially varying probe intensity this acts as a dipole trap. Herein lies the apparent dilemma: the choice of bright beams (at large detuning) comes at the cost of an undesired dipole potential. The alternative of dim probe beams (at small detunings) minimizes the dipole force but poses the challenge of low-noise wideband photodetection. In some cases, dipole forces are not a problem, e.g., warm vapors whose temperature is much larger than the scalar light shift, or cold atoms in deep optical lattices [33], but experiments with ultracold samples that are weakly confined (i.e., not in lattices) are acutely affected by probe dipole forces.

C. Backaction dipole forces

There are several approaches for reducing the dipole force effects arising from the scalar coherent backaction of the Faraday probe. A uniform intensity probe exerts no dipole force: making the probe beam very large compared to the sample approaches this limit. The fraction of the incident probe beam that interacts with the atoms is then very small; in Ref. [3], a 1-mm-waist probe illuminated a Bose-Einstein condensate (BEC) of Thomas-Fermi radius less than 10 μm, meaning that of the intense 50 mW incident beam less than 5 μW arrived at the polarimeter. A possible alternative, not attempted to our knowledge, is to shape the beam into a flat-topped profile with specialized diffractive or refractive optics. Superposing a second "probe" beam detuned to the other side of resonance can cancel the scalar (and potentially tensor) light shifts [35], at the expense of additional complexity and reduced SNR due to the additional off-resonant scattering (unless the second beam is also photodetected).

Here we show that it is possible to perform Faraday detection of an alkali ground-state spin with zero scalar light-shift backaction on the atoms, using a single-frequency laser beam focused to a Gaussian waist matched to the atomic sample. We exploit the fine structure of the alkali principal series ($^2S \rightarrow {}^2P$) transitions, tuning our Faraday probe near a "magic-zero" or "tune-out" wavelength of 790.018 nm [36], the line-strength-weighted midpoint of the doublet. At this wavelength, the scalar light shift vanishes [37] but, critically, the Faraday rotation contributions from the D_1 and D_2 lines reinforce. While operating at the magic-zero wavelength requires very intense beams, we show that this is achieved with reasonable optical powers that are near optimal for broad-bandwidth shot-noise limited photodetection.

D. Outline

In Sec. II, we consider the spherical decomposition of the dipole interaction in the far-detuned limit. We discuss the requirements for nulling induced light shifts of the Faraday probe and consider the location of several magic-zero wavelengths. Comparative expressions for the SNR are derived in three different regimes, from which we can identify an optimal choice of magic-zero wavelength for a minimally perturbative shot-noise limited Faraday measurement. In Sec. III, we outline the technical details of our spinor quantum gas and Faraday measurement apparatus. In Secs. IV and V, we describe the signal processing and optimization of our Faraday measurement via the cancellation of probe-induced light shifts and suppression of ambient magnetic field gradients. In this analysis, we introduce the use of spectrograms for precisely evaluating the Larmor frequency, SNR, and for characterizing the amplitude and frequency modulation created by ambient magnetic fields gradients and noise, and spin-dependent collision dynamics.

II. BACKGROUND THEORY

A. Atom-light interaction

In the far-detuned limit, the atom-light dipole interaction is well described by an effective polarizability Hamiltonian that describes stimulated Raman transitions between the ground states. A spherical tensor decomposition allows this interaction Hamiltonian to be written in terms of the probe-beam Stokes operators $\hat{S}_i$ and the atomic spin operators $\hat{F}_i$ [38–40]. Following [38], the scalar, vector, and tensor contributions can be separated as

$$\hat{\mathscr{H}}_{\rm int} = \hat{\mathscr{H}}^{(0)}_{\rm int} + \hat{\mathscr{H}}^{(1)}_{\rm int} + \hat{\mathscr{H}}^{(2)}_{\rm int}, \tag{1}$$

$$\hat{\mathscr{H}}^{(0)}_{\rm int} = g \sum_{J'F'} \frac{\alpha^{(0)}_{J'F'}}{\Delta_{J'F'}} \frac{2}{3} \hat{S}_0, \tag{2}$$

$$\hat{\mathscr{H}}^{(1)}_{\rm int} = g \sum_{J'F'} \frac{\alpha^{(1)}_{J'F'}}{\Delta_{J'F'}} \hat{S}_z \hat{F}_z, \tag{3}$$

$$\hat{\mathscr{H}}^{(2)}_{\rm int} = g \sum_{J'F'} \frac{\alpha^{(2)}_{J'F'}}{\Delta_{J'F'}} \big\{ \hat{S}_x \big(\hat{F}_x^2 - \hat{F}_y^2\big) + \hat{S}_y (\hat{F}_x \hat{F}_y + \hat{F}_y \hat{F}_x) + \hat{S}_0 \big[3\hat{F}_z^2 - F(F+1)\big]/3 \big\}, \tag{4}$$

where $g = \omega/2\epsilon_0 V$, ω is the probe frequency, V is the quantization volume, and $\Delta_{J'F'}$ is the probe detuning above resonance. The sums are over all excited states $|J'F'\rangle$ permitted by dipole transitions from the ground state $|JF\rangle$, with the coupling strengths $\alpha^{(i)}_{J'F'}$ in this convention defined in Appendix A.

Unlike similar treatments, the explicit J' dependence allows consideration of large detunings where multiple fine-structure transitions contribute. In particular, we consider the net effect of the D_1 ($J' = \frac{1}{2}$) and D_2 ($J' = \frac{3}{2}$) transitions on the $F = 1$ hyperfine states of ^{87}Rb.

The scalar interaction $\hat{\mathscr{H}}^{(0)}_{\rm int}$ gives rise to a state-independent energy shift, which can be eliminated by tuning the probe to a magic-zero or tune-out wavelength [37,41,42]. Magic-zero wavelengths exist between each pair of adjacent resonances: at specific detunings within the hyperfine manifold or between the fine-structure transitions (Fig. 1). Tuning the probe to one of these wavelengths prevents any dipole forces arising from

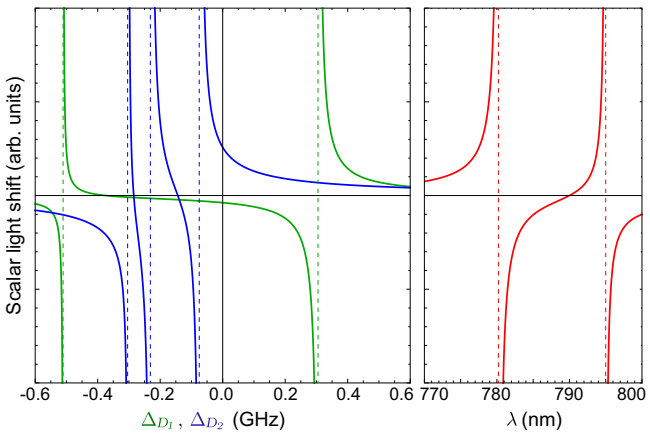

FIG. 1. Scalar light shift (arising from $\hat{\mathscr{H}}^{(0)}_{\rm int}$) for ^{87}Rb atoms in $F = 1$ near the D_1 (green) and D_2 (blue) lines, and between the two (red) lines, showing the detunings relative to respective fine-structure transitions (left) and wavelengths (right) at which the scalar interaction vanishes.

the spatially inhomogeneous spatial profile, which is beneficial for long interrogation times.

The vector contribution $\hat{\mathscr{H}}^{(1)}_{\rm int}$ represents a coupling between the Stokes vector of the light and the atomic spin. A perfectly linearly polarized probe has $\langle \hat{S}_z \rangle = 0$ and results in no vector light shift for the atoms as it causes no evolution of the atomic spin operator $\hat{\boldsymbol{F}}$.

However, spin-polarized atoms will cause evolution of the Stokes vector as the probe light propagates through: the Faraday effect. This corresponds to rotation of the probe polarization by an angle $\varphi_z = \varphi_0 \langle \hat{F}_z \rangle / \xi_f$, where

$$\varphi_0 = \frac{\pi \alpha_0 \tilde{\rho}}{\epsilon_0 \hbar \lambda}, \quad \frac{1}{\xi_f} = \sum_{J'F'} \frac{\alpha^{(1)}_{J'F'}}{\alpha_0 \Delta_{J'F'}}, \tag{5}$$

$\tilde{\rho}$ is the atomic column density, λ is the probe wavelength, and α_0 is the polarizability constant as derived in Appendix A. We term ξ_f the "coherent weighted detuning", which accounts for the different coupling strengths of different atomic transitions. The quantity φ_0 can alternately be expressed in terms of the on-resonant optical depth ($D_{\rm opt}$) of any transition $|J\rangle \to |J'\rangle$ as [43]

$$\varphi_0 = \frac{\lambda_{J'}}{\lambda} \frac{\Gamma_{J'}}{4} D_{\rm opt}, \tag{6}$$

where $D_{\rm opt} = \tilde{\rho}\, \sigma_{J'}$ and $\sigma_{J'} = 3\lambda^2_{J'}/2\pi$ is the resonant cross section.

The tensor interaction $\hat{\mathscr{H}}^{(2)}_{\rm int}$ results in complicated evolution of the atomic spin [32]. For detunings much larger than the excited-state hyperfine splittings, it scales as $O(F^2 \gamma_s)$ where γ_s is the scattering rate. The constant of proportionality is of the order of unity [44] and so the tensor light shift is negligible in $F = 1$ for measurement times much less than the scattering lifetime $1/\gamma_s$. The tensor light shift can be eliminated in pulsed measurement using dynamical decoupling [45], and in general the interaction vanishes when the probe polarization is oriented at $\arctan(\sqrt{2}) = 54.7^\circ$ with respect to the external magnetic field [32].

Choice of the probe polarization and detuning therefore allows the undesirable terms of the polarizability Hamiltonian to be eliminated, leaving only the Faraday interaction that probes the atomic spin state. This is significant as the spatially varying probe-beam intensity profile would otherwise cause spatially dependent light shifts that would dephase the atomic spins.

B. Signal-to-noise optimization

A balanced polarimeter splits the probe beam into its polarization components, with respective intensities

$$I_\pm = I_0 \cos^2\left(\frac{\pi}{4} \pm \varphi_z\right) \to I_+ - I_- \approx 2 I_0 \varphi_z \quad \text{for} \quad \varphi_z \ll 1. \tag{7}$$

We allow transverse variation in the probe-beam intensity I_0 and column density of the atoms $\tilde{\rho}$, but suppress parameters for brevity. The polarimeter signal is then $P_+ - P_- = 2\kappa \int_\Omega I_0 \varphi_z \, dA$, where Ω is the effective detection aperture at the position of the atoms, and κ is the net optical transmission from atoms to detector, which accounts for losses at optical elements and the quantum efficiency of the detector.

Measurement of the spin projection is limited by intensity fluctuations in the probe beam, which contain contributions from technical noise and photon shot noise. A perfectly balanced polarimeter removes the technical noise but cannot remove the shot noise; the root-mean-square (RMS) shot noise across the measurement interval τ_f is $P_n = \sqrt{\hbar \omega P_{\rm det}/\tau_f}$, where $P_{\rm det} = \kappa \int_\Omega I_0 \, dA$ is the total detected power.

Following the approach of Smith *et al.* [33], we define the SNR as the ratio of inferred spin projection to the associated RMS fluctuations caused by shot noise in the probe,

$$\mathrm{SNR} \equiv \frac{|\langle \hat{F}_z \rangle|}{\delta \hat{F}_z} = \frac{|P_+ - P_-|}{P_n} = \frac{2\kappa |\langle \hat{F}_z \rangle|}{\xi_f P_n} \int_\Omega I_0 \varphi_0 \, dA. \tag{8}$$

The SNR can therefore be improved by increasing the intensity I_0 or detuning closer to resonance to reduce ξ_f. However, both increase off-resonant scattering of probe photons, limiting the duration of the measurement. We therefore consider optimizing the SNR at a fixed scattering rate γ_s by appropriate choice of P_0, and varying the detuning.

The scattering rate γ_s for a given probe intensity I_0 is estimated with the Kramers-Heisenberg relation in Appendix B. Summing over all intermediate excited states within the fine-structure doublet gives $\gamma_s = \gamma_0 I_0 / \xi_s^2$, where

$$\gamma_0 = \frac{\omega^3 \alpha_0^2}{18\pi \epsilon_0^2 \hbar^3 c^4} \quad \text{and} \quad \frac{1}{\xi_s^2} = \sum_{J'F'} \frac{\alpha^{(0)}_{J'F'}}{\alpha_0 \Delta^2_{J'F'}}. \tag{9}$$

We term ξ_s the "incoherent weighted detuning" accounting for different scattering rates on different transitions.

The scattering lifetime τ_s of the cloud is the inverse of the density-weighted average of scattering rates across the cloud,

$$\frac{1}{\tau_s} \equiv \int_\infty \gamma_s \frac{\tilde{\rho}}{N} \, dA = \frac{\gamma_0}{N \xi_s^2} \int_\infty I_0 \tilde{\rho} \, dA, \tag{10}$$

where $\int_\infty \ldots$ indicates integration over all space, and N is the total number of atoms in the cloud. The SNR can then be

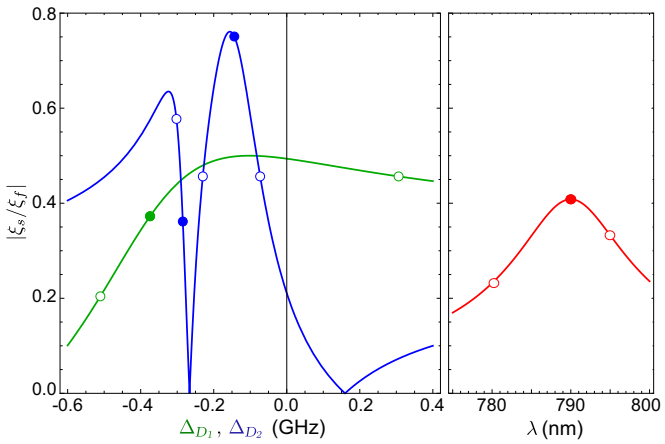

FIG. 2. Atomic component of the SNR for detunings near the D_1 (green) and D_2 (blue) lines (left) vs between the two lines (right). Open circles correspond to hyperfine-structure (left) or fine-structure (right) resonances; closed circles correspond to magic-zero wavelengths. Constructive (destructive) interference between the Faraday rotation contributions from adjacent transitions leads to a maximum (zero) in $|\xi_s/\xi_f|$ at $\Delta_{D_2}/2\pi = -0.16\,(-0.27)$ GHz. Near-resonant effects (at detunings less than the natural linewidth) are not accounted for by Eq. (1) or included in this plot.

written as

$$\mathrm{SNR} = \sqrt{3\kappa}N\sqrt{\frac{\sigma_0}{\mathcal{A}}}\left|\frac{\xi_s}{\xi_f}\right|\sqrt{\frac{\tau_f}{\tau_s}}|\langle\hat{F}_z\rangle|, \tag{11}$$

where $\sigma_0 = 3\lambda^2/2\pi$ is the dipole cross section and $\mathcal{A}$ is an effective aperture area accounting for the spatial profiles of the atom cloud and probe beam,

$$\mathcal{A} = \frac{\int_\Omega I_0\,dA\int_\infty I_0\frac{\tilde{\rho}}{N}\,dA}{\left(\int_\Omega I_0\frac{\tilde{\rho}}{N}\,dA\right)^2}, \tag{12}$$

where $\tilde{\rho}/N$ is the normalized column density for which $\int_\infty \tilde{\rho}/N\,dA = 1$. Equation (11) clearly separates the SNR into the expected dependencies on atom number, quantum efficiency, and spin projection, and on three ratios: a spatial ratio $\sigma_0/\mathcal{A}$ of atomic cross section to detection area, an atomic structure ratio ξ_s/ξ_f depending only on detuning within the doublet and quantum numbers (see Fig. 2), and the ratio of measurement time to scattering time τ_f/τ_s.

If the probe intensity is constant across the detection aperture, the effective aperture area is $\mathcal{A} = A(N/N_a)^2$, where $N_a = \int_\Omega \tilde{\rho}\,dA$ is the number of atoms contributing to the measurement and A is the physical aperture area. The SNR can then be written

$$\mathrm{SNR} = \sqrt{3\kappa}N_a\sqrt{\frac{\sigma_0}{A}}\left|\frac{\xi_s}{\xi_f}\right|\sqrt{\frac{\tau_f}{\tau_s}}|\langle\hat{F}_z\rangle|. \tag{13}$$

The optimum aperture Ω is obtained by maximizing $N_a/\sqrt{A}$ for a given atomic column-density distribution ρ/N. For a cylindrically symmetric Gaussian cloud with transverse $1/e^2$ radius R, the optimum radius a of a circular aperture is $a = 0.79R$, whereas for a Thomas-Fermi cloud with radius R, it is $a = 0.73R$.

C. Distinct detuning regimes

The atomic dependence of the SNR as a function of detuning is captured in the ratio ξ_s/ξ_f. We now consider a ^{87}Rb condensate in $F = 1$ with probe detuning in one of three regimes: (I) near a single fine-structure line, (II) between the two lines, and (III) within the hyperfine structure of a single line.

Regime I. For probe detuning near the D_2 line ($|\Delta_{D_2}| \ll |\Delta_{D_1}|$), but far detuned with respect to the excited-state hyperfine splitting, $\xi_f \approx 3\sqrt{2}\,\xi_s$, and

$$\mathrm{SNR}_{(D_2)} = \frac{\lambda N_a\sqrt{\kappa}}{2\pi a}\sqrt{\frac{\tau_f}{\tau_s}}, \tag{14}$$

where a circular aperture of radius a has been assumed. This is congruent with the "single-line" expression in Ref. [33], which considered a Gaussian cloud profile with optimum aperture and homogeneous illumination.

Regime II. In the far-detuned limit between the D_1 and D_2 lines, the dependence of the SNR is captured in the ratio

$$\frac{\xi_s}{\xi_f} \approx \frac{\Delta_{D_1}^{-1} - \Delta_{D_2}^{-1}}{3\sqrt{\Delta_{D_1}^{-2} + 2\Delta_{D_2}^{-2}}} = \frac{(2/\sqrt{3})\omega_{\mathrm{fs}}}{\sqrt{(6\Delta + \omega_{\mathrm{fs}})^2 + 8\omega_{\mathrm{fs}}^2}}, \tag{15}$$

where $\Delta = \frac{1}{2}(\Delta_{D_1} + \Delta_{D_2})$ is the detuning from the center of the lines and ω_{fs} is the fine-structure splitting. The Faraday contributions from each line add coherently, but the scattering contributions add in quadrature.

This expression is maximized at $\Delta = -\omega_{\mathrm{fs}}/6$, giving $\lambda = 790.0$ nm and $\xi_s/\xi_f = \sqrt{2}/3$. This detuning is precisely where the scalar polarizability vanishes (a magic-zero wavelength). Measurement at this wavelength is fortuitously doubly optimal in terms of both SNR and minimizing the trap perturbation discussed previously.

Regime III. When detuning between hyperfine transitions of the D_2 line (Fig. 2), the SNR is maximized at $\Delta_{D_2}/2\pi = -156$ MHz with $|\xi_s/\xi_f| = 0.76$, which does not correspond to a magic-zero wavelength. There is therefore a trade-off between SNR and induced scalar light-shift perturbation. Choosing the magic-zero wavelength at $\Delta_{D_2}/2\pi = -143$ MHz eliminates this perturbation with a nominal decrease in SNR arising from $|\xi_s/\xi_f| = 0.75$.

In comparing the above three regimes as candidates for a minimally perturbative atom-light interface, Regime I is discounted as it has no proximate magic-zero wavelength. In principle, there appears to be little advantage between operating at magic-zero wavelengths in Regimes II and III, as the $|\xi_s/\xi_f|$ ratios are similar. However, the closer detuning in Regime III necessitates a 10^5 reduction in probe power to achieve the same scattering rate as in Regime II, making continuous shot-noise limited photodetection far more challenging. This motivates Regime II to perform continuous Faraday probing, which we exclusively consider hereafter.

III. APPARATUS

Our spinor Bose-Einstein condensate (BEC) apparatus [46] loads 3×10^9 ^{87}Rb atoms in a six-beam magneto-optical trap from a Zeeman slower. The laser-cooled atoms are optically pumped into the $|F = 1, m_F = -1\rangle$ state before they are evaporatively cooled in different conservative potentials: first

a hybrid magnetic optical dipole trap [47], followed by a crossed-beam dipole trap formed using a 20 W fiber laser at 1064 nm. Care was taken to extinguish vector-light shifts from the dipole trapping light [48], which would otherwise result in a Zeeman-state-dependent confining potential and premature dephasing of the collective condensate spin. The BEC is typically comprised of 3×10^5 atoms, held in a harmonic potential with trap frequencies (35,60,80) Hz. Three orthogonal sets of coil pairs generate magnetic fields of up to 20 G, with individual control over the current in each coil enabling the generation of magnetic field gradients. Conventional time-of-flight absorption imaging is routinely used for diagnostic purposes such as optimizing the cooling and trapping that precedes Faraday detection. Alternatively, an absorption image of the cloud can be taken after it has been dispersively interrogated in-trap with the off-resonant probe to measure number loss and observe any changes in cloud structure.

The probe light is generated with a diode laser tuned near 790 nm, with up to 16 mW reaching the science chamber. The probe is tuned using a HighFinesse WSU-10 wave meter with a short-term stability of 10 MHz. Active frequency stabilization is not required due to insensitivity of the atom-light interaction so far from resonance, requiring only temperature stabilization.

Despite lasing near 790 nm, the diode laser producing the Faraday beam has a broad amplified spontaneous emission (ASE) background that spans 770–810 nm. This background emission is weak, but contains a small component that is resonant with the atomic transitions at 780 nm (D_2 line) and 795 nm (D_1 line), significantly decreasing the BEC lifetime. An interference filter blocks the resonant components increasing the $1/e$ lifetime from 30 ms to 1.2 s for 9.7 mW of probe power. Measurements of the BEC lifetime at various probe-beam powers yield a scattering rate of 85(1) s^{-1} W^{-1} for $\lambda = 790.0$ nm, consistent with Eq. (10). These measurements account for the dominant collisional-loss mechanisms: three-body collisions between condensate atoms [49] and one-body collisions with background atoms in the vacuum. The one-body limited lifetime in the absence of probe light is 35 s.

The probe beam is focused to a 150 μm $1/e^2$ diameter at the BEC (geometric mean Thomas-Fermi radius 19 μm) for near-uniform illumination of the atoms. Limited optical access requires relay lenses to collect the transmitted probe light, which is magnified by a microscope objective and reimaged onto a iris aperture to block light not interacting with the BEC (Fig. 3). The Faraday probe beam, aperture, and trapped condensate are coaligned by coupling resonant light into the same beam path and performing in-trap absorption imaging with a machine-vision CCD camera.

A. Scalar light shift

The manifestation of probe-induced scalar light shifts varies across platforms and can confound experiments seeking to emulate condensed-matter phenomena with ultracold atoms [5]. Here, we study the kinematic manifestation of the probe-induced scalar light shift as a general representation of such deleterious effects.

We measure the dipole force during a 1.2 ms pulse of probe light applied to the condensate immediately after releasing it from the 1064 nm dipole trapping potential. The resulting

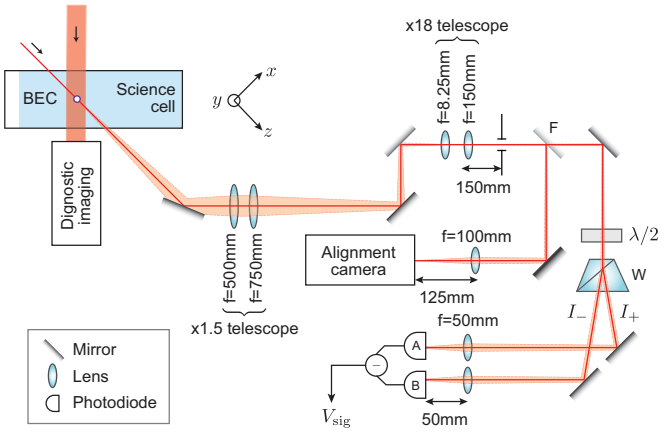

FIG. 3. Faraday atom-light interface: the probe is focused onto the condensate, then magnified and reimaged onto an iris to aperture the beam. A flipper mirror (F) reflects the beam to either a camera or balanced polarimeter formed by a Wollaston prism (W) and dual-port differential photodetector (A-B).

impulse is proportional to the probe intensity gradient at the condensate, and was measured by observing the displacement of the magnetically insensitive $m_F = 0$ Zeeman component after 21 ms of subsequent freefall.

In Fig. 4 (top), we plot the measured impulse for wavelengths between the two lines; cf. Regime II in Sec. II C. The probe-induced impulse is seen to cross through zero at the magic wavelength; the lowest measured impulse was $-0.001 \pm 0.024\,\hbar k$ at $\lambda = 790.009$ nm where $k = 2\pi/\lambda$. Across this wavelength range, the measured SNR for fixed scattering rate (Fig. 4, bottom) varies very little ($\sim$1 dB), in agreement with theoretical prediction. This confirms that $\lambda = 790.0$ nm is ideal for minimally perturbative continuous Faraday probing, and we use this probe wavelength for all measurements below.

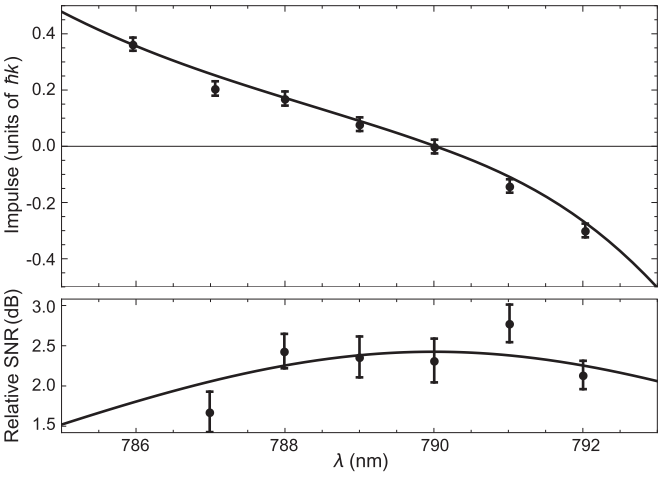

FIG. 4. Top: Impulse imparted to an untrapped Bose-Einstein condensate by a 21 ms exposure to the probe-beam scalar light shift, as a function of wavelength. The solid line is the theoretical prediction based on Eq. (2), with only intensity gradient (a multiplicative constant) as a free parameter. Bottom: SNR relative to the near-resonant (D_2 line) SNR for the same scattering rate. The solid line is equivalent to the SNR plotted in Fig. 2.

B. Faraday probe polarimetry

The polarization rotation is measured using a Wollaston prism placed upstream from a differential photodetector [50] using large-area (13 mm^2) Hamamatsu S1223-01 photodiodes, chosen for their relatively low capacitance. The detector has a transimpedance gain of 1 V/mA with an ac-coupled 100× second-stage amplifier and a variable-gain third-stage voltage amplifier to match the input voltage range of the data-acquisition hardware. The measured noise-equivalent power is 140 μW in a bandwidth of 8 MHz. Optical losses and the detection aperture result in 2 mW of probe light typically recorded on each photodiode.

C. Measurement protocol

The BEC is initially spin polarized along the $+y$ axis in a uniform magnetic field of $B_y = 1$ G, perpendicular to the propagation axis of the probe beam. In this configuration, $\langle \hat{F}_z \rangle = 0$ and the Faraday probe experiences no polarization rotation. The probe is switched on for 20 ms to ascertain the photon shot noise, before tipping the spins into the x–z plane with a resonant radio-frequency $\frac{\pi}{2}$ pulse, initiating Larmor precession and the generation of a Faraday signal at the Larmor frequency f_L. The analog signal produced by the photodetector is digitized by a National Instruments PCIe-6363 16-bit analog-to-digital converter (ADC) with a maximum acquisition rate of 2 MS/s [51].

IV. SIGNAL STRUCTURE AND OPTIMIZATION

The raw measured polarimeter signal is dominated by photon shot noise and low-frequency thermal fluctuations (Fig. 5, top). Applying a band-pass filter around the Larmor frequency reveals the Faraday signal (Fig. 5, middle), which exhibits multiple decays and revivals within an overall free-induction decay (FID) envelope.

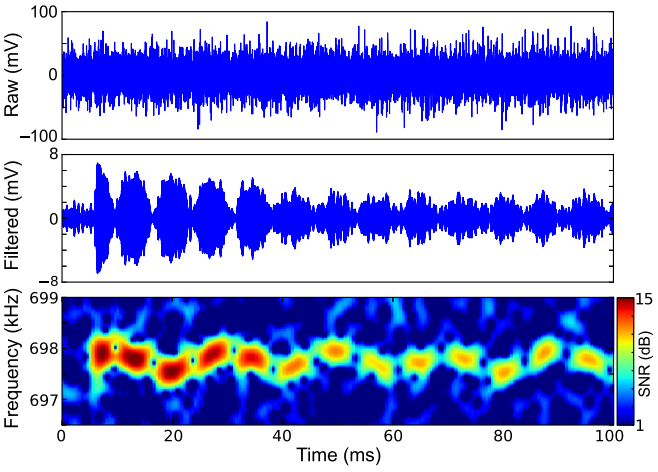

FIG. 5. Typical raw polarimeter signal (top) buried in noise, which is reduced by a 10 kHz band-pass filter to obtain the Faraday signal (middle) showing periodic revival. A spectrogram reveals both amplitude and frequency modulation of the Faraday signal (bottom). The false color represents signal-to-noise ratio (SNR) and is shared by all spectrograms presented hereafter. The average Larmor frequency is $f_L = 697.8(4)$ kHz.

More structure is revealed using a short-time Fourier transform (STFT) algorithm, which divides the signal into overlapping "windows" and combines the magnitude of the Fourier transforms of each window into a spectrogram (Fig. 5, bottom). The Gabor limit defines a trade-off between frequency and temporal resolution. The present analysis oversamples in both time and frequency; overlapping rectangular 5 ms windows are taken every 1 ms and zero padded before Fourier transforming. This smooths the spectrogram which clearly demonstrates both amplitude and frequency modulation, which is not clear from the bandpass-filtered time-domain signal.

A. Quadratic Zeeman shifts

The primary cause of amplitude modulation is the quadratic Zeeman effect (QZE), which cannot be neglected for strong bias fields and long interrogation times.

In the single-mode approximation, the spinor wave function is $(\sqrt{\rho_-}e^{i\Theta_-}, \sqrt{\rho_0}e^{i\Theta_0}, \sqrt{\rho_+}e^{i\Theta_+})$, where ρ_i and Θ_i are the fractional populations and phases of the Zeeman sublevels. Spin-polarized states with $\rho_+ = \rho_-$ maximize $\langle \hat{F}_z \rangle$, and therefore the induced Faraday signal [Eq. (11)]. The spin projection evolves under the mean-field Hamiltonian including spin exchange as [52]

$$\begin{aligned}
\langle \hat{F}_z \rangle &= 2\sqrt{\rho_0(1-\rho_0)}\cos\left(\frac{1}{2}\Theta\right)\cos(\omega_L t),\\
\frac{\partial \rho_0}{\partial t} &= \tfrac{2c}{\hbar}(1-\rho_0)\sin\Theta,\\
\frac{\partial \Theta}{\partial t} &= -2q_z + \frac{2c}{\hbar}(1-2\rho_0)(1+\cos\Theta),\\
\omega_L &\equiv (E_{+1} - E_{-1})/2\hbar,\\
q_z &\equiv (E_{+1} + E_{-1} - 2E_0)/2\hbar,
\end{aligned} \tag{16}$$

where $\Theta = \Theta_+ + \Theta_- - 2\Theta_0$ is the spinor phase, E_m is the energy of the $|F,m\rangle$ state, $c \propto a_2 - a_0$ is a spin-mixing coefficient, and a_f are the elastic scattering lengths for two $F = 1$ atoms colliding with total spin f.

This result demonstrates that the spin projection $\langle \hat{F}_z \rangle$ and therefore the Faraday signal oscillates at ω_L, which is linear in B to $O(B^3)$. However, the signal is amplitude modulated directly through the cosine term, and indirectly through fluctuations in ρ_0 arising from spin mixing. When the QZE dominates ($q_z \gg c/\hbar$), the spinor phase winds linearly, $\Theta = 2q_z t$, and fluctuations in ρ_0 are "frozen out" with $\rho_0 = 1/2$. Consequently, $\langle \hat{F}_z \rangle$ and the Faraday signal is amplitude modulated at q_z [53].

Nonlinear Zeeman shifts are a common problem in optical magnetometry and are addressed using a variety of techniques [20]. In our system, such shifts cause coherent spin evolution and do not limit measurement duration. However, truly continuous magnetometry requires that this amplitude modulation be suppressed.

This can be achieved at arbitrary magnetic field strengths by applying off-resonant microwave coupling [54] detuned from the $|F = 1, m_F = 0\rangle \leftrightarrow |F = 2, m_F = 0\rangle$ transition. For microwaves with Rabi frequency $\Omega_{\rm mw}$ and detuning

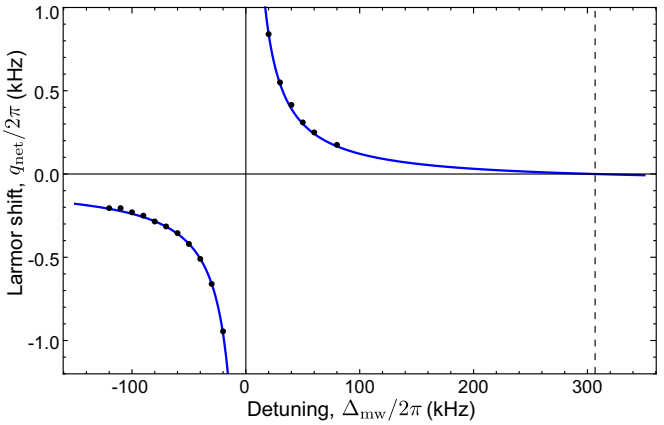

FIG. 6. Measured effective quadratic shift $q_{net} = q_z - q_{mw}$ in the presence of microwaves detuned by Δ_{mw} above the $|F = 1, m_F = 0\rangle \leftrightarrow |F = 2, m_F = 0\rangle$ clock transition at $f = 6\,834\,682\,610.904$ Hz. The effective shift vanishes at $\Delta_{mw}/2\pi = 307(2)$ kHz (dashed line) and the inferred microwave Rabi frequency is $\Omega_{mw}/2\pi = 8.50(2)$ kHz.

$|\Delta_{mw}| \gg \Omega_{mw}$, the population of $F = 2$ is minimal, and the induced quadratic shift is $q_{mw} \approx -\Omega_{mw}^2/4\Delta_{mw}$ [55]. Hence the QZE can be suppressed by appropriate choice of the microwave detuning (Fig. 6), as q_z is consistent with the Breit-Rabi equation [56].

B. Vector light shifts

Amplitude modulation also arises from imperfect linear polarization of the probe beam causing evolution of the atomic spin state through the vector light shift. Spatial variation of the probe intensity renders this an effective magnetic field gradient [48], which dephases the collective spin and limits the measurement time.

This dephasing can be eliminated by using a uniform intensity probe or making the polarization perfectly linear. Although the polarization of the probe is purified using a Glan-Laser polarizer (extinction $10^5 : 1$) before the vacuum window, birefringence of optical elements after this polarizer causes an elliptically polarized probe at the atoms. In the quasistatic approximation, Eq. (3) can be rewritten

$$\hat{\mathcal{H}}_z = \frac{\mu_B g_F}{\hbar} B_{vls} \hat{F}_z, \tag{17}$$

where $B_{vls} \propto \langle \hat{S}_z \rangle$ is the effective magnetic field in the z direction induced by the probe-beam ellipticity.

A quarter-wave plate at angle θ before the science cell enables control of the ellipticity within the cell through $B_{vls} = B_{vls}^{(0)} \sin[2(\theta - \theta_0)]$, where $B_{vls}^{(0)}$ is the vector light shift (VLS) for a circularly polarized probe and θ_0 is the wave-plate angle at which the polarization is linear at the atoms. B_{vls} introduces a small shift to the Larmor frequency,

$$\omega_L = \frac{\mu_B g_F}{\hbar} \sqrt{B_y^2 + (B_z + B_{vls})^2}, \tag{18}$$

where B_y is the dominant bias field component and B_z is the (small) background field component in the z direction. The measurement is sufficiently sensitive that the VLS component

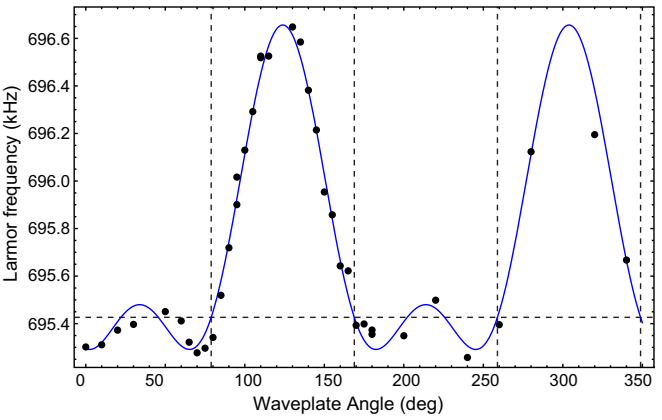

FIG. 7. Larmor frequency as a function of $\lambda/4$ wave-plate angle (θ), showing the shift induced by the VLS and the angles at which the VLS vanishes (dashed lines). The background field component is $B_z = 19.6(8)$ mG, maximum VLS strength is $B_{vls}^{(0)} = 43(1)$ mG, and $\theta_0 = 78.9(4)$ deg.

can be extracted as a function of θ, and hence θ_0 determined (Fig. 7).

V. MICROSCALE ATOMIC MAGNETOMETRY AT HIGH TEMPORAL RESOLUTION

With the primary sources of amplitude modulation eliminated, we achieve continuous magnetometry (Fig. 8) revealing time-dependent magnetic field fluctuations integrated across the $(30\,\mu m)^3$ sensing volume of the atomic condensate. This time dependence is manifest as frequency modulation of the Faraday signal, in this instance containing odd harmonics of the 50 Hz power-line frequency due to nearby electronic equipment.

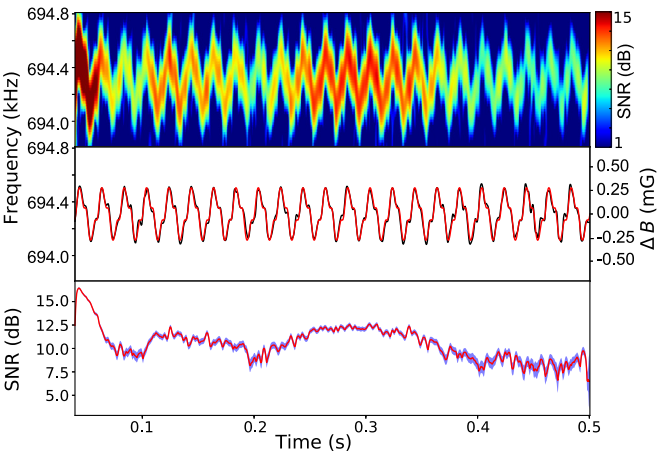

FIG. 8. Spectrogram with QZE eliminated (top) enables continuous measurement of the Larmor frequency (middle) for time-dependent magnetometry. Larmor frequency from peak fitting in each spectrogram window (middle, black); this frequency modulation is modeled by the first three harmonics of the power line (red). Measuring the peak SNR at each spectrogram window (bottom) clearly shows a residual amplitude-modulation signal, which we attribute to ambient magnetic field gradients.

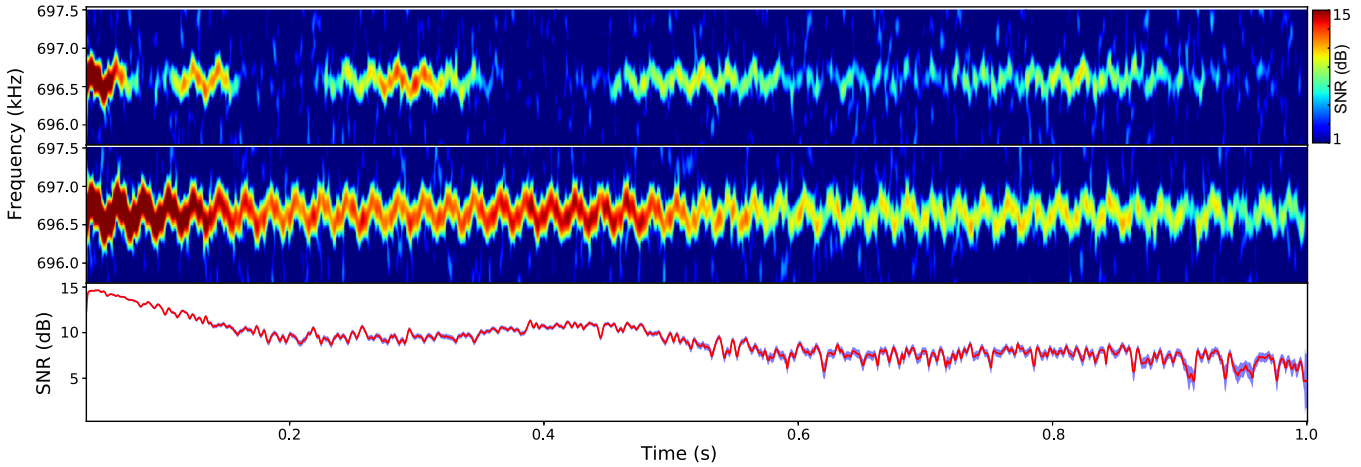

FIG. 9. Measured Faraday signal without (top) and with (middle) cancellation of both VLS and background magnetic field gradients showing (bottom) gradual decay of the SNR over a 1 s measurement duration. Top: The quadratic Zeeman shift has been canceled using microwave dressing (Sec. IV), but magnetic field gradients due to vector light shifts and background fields remain. We contend that the irregular amplitude modulation is due to the rich dynamical interplay between these gradients, spin-mixing dynamics of the condensate, and the concomitant breakdown of the single-mode approximation. Middle: Ensuring linear polarization of the probe light and applying a countergradient results in reduced dephasing and achieves long-lived continuous readout of the spin projection. Bottom: Prolonged SNR exceeding unity beyond 1 s. Off-diagonal gradients $\lesssim$1 mG/cm which were not canceled result in coherent decay and revival of the cloud, causing the residual amplitude modulation.

The peak-to-peak variation of this pickup is $\Delta B_{\rm ac} \approx 558(4)\,\mu$G. We resolve the harmonic components of the time-varying magnetic field, finding amplitudes of 162(1), 46(1), and 7(1) μG at 50, 150, and 250 Hz, respectively.

The spectrogram (Fig. 8, top) shows evidence of residual amplitude modulation, which is clarified by plotting the peak amplitude in each time window (Fig. 8, bottom). The remaining free-induction decay of the signal is caused by the small gradients in real magnetic fields, as opposed to light-induced gradients nulled in Sec. IV. A spherical cloud of radius R has dephasing time scale $\tau_D \sim \pi/2\gamma bR$, where $b = \sum_i \partial B_y/\partial x_i$ in a y-oriented magnetic field. The ambient gradients in our apparatus were found to be $\sim$10 mG/cm, measured independently using a differential Ramsey interferometer [46], resulting in a dephasing time of $\tau_D \sim 20$ ms. To achieve continuous magnetometry on the time scale of seconds, we apply a countergradient $\partial B_y/dy$ using asymmetric currents in the bias magnetic field coils. The resulting free-induction decay (Fig. 9) shows an SNR exceeding unity beyond 1 s. The gradient was nulled to within $b \lesssim 1$ mG/cm ($\tau_D \sim 200$ ms), limited by off-diagonal gradients (e.g., $\partial B_y/dz$). These can only be canceled using a specific arrangement of gradient coils [46] not available in this experiment.

We determine the initial SNR to be 16.3(2) dB from the spectrogram data shown in Fig. 8 [57]. For a Thomas-Fermi density profile and Gaussian probe beam, Eq. (11) predicts a shot-noise limited SNR of 18.3 dB provided $N = 3 \times 10^5$ atoms, optical transmission $\kappa = 0.2$, aperture radius $a = 38\,\mu$m equal to twice the geometric-mean Thomas-Fermi radius, $|\xi_s/\xi_f| = \sqrt{2}/3$, and scattering lifetime $\tau_s = 1.2$ s. By recomputing spectrograms with different window length τ_f, we confirmed that the measured SNR scales with $\sqrt{\tau_f}$ as predicted.

The ratio of the atomic standard quantum limit (SQL) to the photon shot-noise limit in Eq. (8) can be expressed as $(\delta\hat{F}_z)_{\rm SQL}/\delta\hat{F}_z = \sqrt{\kappa\sigma_0\tilde{\rho}\tau_f/(2\tau_s)}$, where σ_0 is the resonant photon-scattering cross section [58].

Our measurement is dominated by photon shot noise for $\tau_f < 12.5$ ms, justifying the analysis in Sec. II B. For our parameters, $(\delta\hat{F}_z)_{\rm SQL} = 0.6\,\delta\hat{F}_z$, which decreases the predicted SNR by 0.7 dB.

The SNR defined in Eq. (8) is the reciprocal of the uncertainty in the Larmor phase of the collective spin $1/\delta\phi$, and can thus be used to estimate the magnetic field sensitivity per unit bandwidth $\delta B\sqrt{T} = 1/(\gamma {\rm SNR}\sqrt{\tau_f})$, where γ is the gyromagnetic ratio. For these data ($\tau_f = 5$ ms), we estimate the photon shot-noise limited field sensitivity to be $\delta B\sqrt{T} = 7\,{\rm pT}/\sqrt{\rm Hz}$, slightly below the experimental value of $10\,{\rm pT}/\sqrt{\rm Hz}$ inferred from the standard error of the fitted Larmor frequency in a given spectrogram window (Fig. 8, middle).

VI. CONCLUDING REMARKS

In conclusion, we have demonstrated continuous Faraday measurement of a condensed spinor gas, absent scalar and vector light shifts. We evaluated the shot-noise limited signal-to-noise ratio for a given scattering rate, motivating the use of a bright, linearly polarized probe at $\lambda = 790$ nm to realize a minimally perturbative atom-light interface.

Spectrogram analysis revealed the detail inherent in the continuous Faraday signal, making plain the quadratic Zeeman effect, vector light shifts, and gradient-induced dephasing as amplitude modulations of the Larmor carrier. We demonstrated how each of these can be canceled in turn, enhancing the contiguous measurement interval without dead time. The resulting long interrogation times of $\sim$1 s enable either close determination of the mean Larmor frequency for precision magnetometry near dc or observation of time-dependent magnetic fields (manifest as frequency modulation of the Larmor

carrier), in accordance with the Gabor limit. Single-shot acquisition of 1 million polarimetry measurements resolved the amplitude of these low-frequency fluctuations to 1 μG in 5 ms intervals, allowing separate harmonic components of parasitic field noise to be identified.

The minimally perturbative nature of the Faraday probe is ideal for quantum state estimation in cold-atomic ensembles [21,22]. In this work, we applied microwave control to null the quadratic Zeeman shift and minimize amplitude modulation of the Faraday signal. The quadratic Zeeman shift breaks the rotational symmetry of the spin degree of freedom, which is necessary to estimate density matrices of spins $>1/2$. To date, quantum state estimators have exploited a fixed quadratic shift borne of a constant probe-laser tensor light shift. Modulating the microwave dressing *during* the measurement will permit pulsed, time-reversible tomographic state reconstruction.

Proposals to apply Faraday quantum nondemolition measurements as momentum-selective probes of strongly correlated quantum gases [5] may founder if the standing wave scalar light shifts (optical lattice) of the probe beam confound the measurand. Implementing these probes at a magic-zero wavelength obviates this impediment, and opens the way to new measurements, including quantum correlation thermometry and continuous Bragg spectroscopy.

In precision magnetometry applications, the long measurement times that we demonstrated open the possibility of single-shot three-axis vector magnetometry by adiabatically rotating the magnetic field bias direction during the measurement.

Real-time data processing of the Faraday signal may be used for closed-loop control of magnetic fields by feedback to compensation coils, for example to suppress fluctuations as required by experiments preparing delicate spin-entangled many-body states.

ACKNOWLEDGMENTS

This work was supported by Australian Research Council (ARC) Grants No. DP1094399 and No. LP130100857, the Australian Postgraduate Award Scheme and a Monash University interdisciplinary research seed grant.

APPENDIX A: INTERACTION COEFFICIENTS

The polarizability coefficients for the $|JF\rangle \rightarrow |J'F'\rangle$ transition are [39]

$$\alpha^{(0)}_{J'F'} = \alpha^{J'F'}_{JF}\left(\delta^{F'}_{F-1} + \delta^{F'}_{F} + \delta^{F'}_{F+1}\right), \tag{A1}$$

$$\alpha^{(1)}_{J'F'} = \alpha^{J'F'}_{JF}\left(-\tfrac{1}{F}\delta^{F'}_{F-1} - \tfrac{1}{F(F+1)}\delta^{F'}_{F} + \tfrac{1}{F'}\delta^{F'}_{F+1}\right), \tag{A2}$$

$$\alpha^{(2)}_{J'F'} = \tfrac{\alpha^{J'F'}_{JF}}{2F'+1}\left(\tfrac{1}{F}\delta^{F'}_{F-1} - \tfrac{2F+1}{F(F+1)}\delta^{F'}_{F} + \tfrac{1}{F'}\delta^{F'}_{F+1}\right), \tag{A3}$$

$$\alpha^{J'F'}_{JF} = \alpha_0(2F'+1)(2J'+1)\left|\begin{Bmatrix} 1 & J & J' \\ I_s & F' & F \end{Bmatrix}\right|^2, \tag{A4}$$

$$\alpha_0 = \frac{3\epsilon_0\hbar\lambda^3_{J'}\Gamma_{J'}}{8\pi^2}, \tag{A5}$$

where δ^n_m is the Kronecker delta, I_s is the nuclear isospin, $\lambda_{J'}$ is the resonant wavelength, and $\Gamma_{J'}$ is the natural linewidth of the transition.

The *polarizability constant* α_0 is independent of J' as $\lambda^3_{D_1}\Gamma_{D_1} = \lambda^3_{D_2}\Gamma_{D_2}$. This can be seen by relating $\Gamma_{J'}$ to the reduced dipole element $\langle J||\boldsymbol{d}||J'\rangle$, expanding in terms of $\langle L||\boldsymbol{d}||L'\rangle$, and evaluating the associated Wigner $6j$.

APPENDIX B: DERIVATION OF SCATTERING RATE

In the far-detuned limit, second-order perturbation theory predicts that an atom in state $|a\rangle$ can transition to state $|b\rangle$ through absorption and emission of a photon via a state $|j\rangle$. For scattering into solid angle $d\Omega$, the Kramers-Heisenberg relation gives the scattering rate as [59]

$$\frac{d\gamma_{a\to b}}{d\Omega} = \frac{I_0\omega^3_{\rm sc}}{(4\pi\epsilon_0)^2\hbar^3c^4}\left|\sum_{|j\rangle}\frac{\langle b|\boldsymbol{\epsilon}_{\rm sc}\cdot\hat{\boldsymbol{d}}|j\rangle\langle j|\boldsymbol{\epsilon}\cdot\hat{\boldsymbol{d}}|a\rangle}{\omega_{ja}-\omega} + \frac{\langle b|\boldsymbol{\epsilon}\cdot\hat{\boldsymbol{d}}|j\rangle\langle j|\boldsymbol{\epsilon}_{\rm sc}\cdot\hat{\boldsymbol{d}}|a\rangle}{\omega_{ja}+\omega_{\rm sc}}\right|^2, \tag{B1}$$

where $\hbar\omega_{ja} = E_j - E_a > 0$ is the energy difference between $|a\rangle$ and $|j\rangle$, I_0 is the probe intensity, ω the probe frequency, $\boldsymbol{\epsilon}$ the polarization vector, and the subscript "sc" denotes the scattered photon.

Taking the probe as linearly polarized, integrating over all emission solid angles $d\Omega$, summing over the scattered photon polarizations q, and all possible final atomic states $|b\rangle$, the total scattering rate out of state $|a\rangle$ is

$$\gamma = \frac{I_0}{6\pi\epsilon_0^2\hbar^3c^4}\sum_{|b\rangle}(\omega-\omega_{ba})^3\sum_q\left|\sum_{|j\rangle}\frac{\langle b|\hat{d}_q|j\rangle\langle j|\hat{d}_0|a\rangle}{\omega_{ja}-\omega}\right|^2. \tag{B2}$$

Applying selection rules, the $q=0$ terms require $F''=F$ and $m''_F = m_F$, so the process is Rayleigh scattering, whereas for $q=\pm1$, $m''_F \neq m_F$ and the process is Raman scattering. Taking $|\omega_{ba}| \ll \omega$ and $\gamma_0 = \omega^3\alpha_0^2/18\pi\epsilon_0^2\hbar^3c^4$, the associated scattering rates for the two processes are

$$\gamma^{(q=0)} = \frac{I_0\gamma_0}{3}\left(\sum_{J'F'}\frac{\alpha^{(0)}_{J'F'}}{\alpha_0\Delta_{J'F'}}\right)^2, \tag{B3}$$

$$\gamma^{(q=1)} + \gamma^{(q=-1)} = 6I_0\gamma_0\left(\sum_{J'F'}\frac{\alpha^{(1)}_{J'F'}}{\alpha_0\Delta_{J'F'}}\right)^2. \tag{B4}$$

This is consistent with a Kramers-Kronig interpretation of the scalar and vector Hamiltonians.

In our system, the total scattering rate can then be calculated using properties of the Wigner-$6j$ symbols as

$$\gamma = I_0\gamma_0\sum_{J'F'}\frac{\alpha^{(0)}_{J'F'}}{\alpha_0\Delta^2_{J'F'}}. \tag{B5}$$

[1] D. Budker and M. Romalis, Nat. Phys. **3**, 227 (2007).

[2] C. A. Muschik, H. Krauter, K. Hammerer, and E. S. Polzik, Quantum Inf. Proc. **10**, 839 (2011).

[3] Y. Liu, S. Jung, S. E. Maxwell, L. D. Turner, E. Tiesinga, and P. D. Lett, Phys. Rev. Lett. **102**, 125301 (2009).

[4] N. Behbood, F. Martin Ciurana, G. Colangelo, M. Napolitano, G. Tóth, R. J. Sewell, and M. W. Mitchell, Phys. Rev. Lett. **113**, 093601 (2014).

[5] K. Eckert, O. Romero-Isart, M. Rodriguez, M. Lewenstein, E. S. Polzik, and A. Sanpera, Nat. Phys. **4**, 50 (2007); M. Mehboudi, M. Moreno-Cardoner, G. D. Chiara, and A. Sanpera, New J. Phys. **17**, 055020 (2015).

[6] T. Isayama, Y. Takahashi, N. Tanaka, K. Toyoda, K. Ishikawa, and T. Yabuzaki, Phys. Rev. A **59**, 4836 (1999).

[7] F. K. Fatemi and M. Bashkansky, Opt. Express **18**, 2190 (2010).

[8] M. Kubasik, M. Koschorreck, M. Napolitano, S. R. de Echaniz, H. Crepaz, J. Eschner, E. S. Polzik, and M. W. Mitchell, Phys. Rev. A **79**, 043815 (2009).

[9] N. Behbood, F. M. Ciurana, G. Colangelo, M. Napolitano, M. W. Mitchell, and R. J. Sewell, Appl. Phys. Lett. **102**, 173504 (2013).

[10] N. Behbood, G. Colangelo, F. Martin Ciurana, M. Napolitano, R. J. Sewell, and M. W. Mitchell, Phys. Rev. Lett. **111**, 103601 (2013).

[11] R. J. Sewell, M. Napolitano, N. Behbood, G. Colangelo, and M. W. Mitchell, Nat. Photon. **7**, 517 (2013).

[12] G. Colangelo, F. M. Ciurana, L. C. Bianchet, R. J. Sewell, and M. W. Mitchell, Nature (London) **543**, 525 (2017).

[13] Y. Liu, E. Gomez, S. E. Maxwell, L. D. Turner, E. Tiesinga, and P. D. Lett, Phys. Rev. Lett. **102**, 225301 (2009).

[14] D. Macaluso and O. M. Corbino, Nuovo Cim. **8**, 257 (1898); D. Macaluso, O. M. Corbino, and L. Magri, *ibid.* **9**, 384 (1899).

[15] Y. Öhman, Stockholms Obs. Ann. **19**, 9 (1956).

[16] W. Kiefer, R. Löw, J. Wrachtrup, and I. Gerhardt, Sci. Rep. **4**, 6552 (2014).

[17] B. Brumfield and G. Wysocki, Opt. Express **20**, 29727 (2012).

[18] A. L. Marchant, S. Händel, T. P. Wiles, S. A. Hopkins, C. S. Adams, and S. L. Cornish, Opt. Lett. **36**, 64 (2011).

[19] W. Zhuang and J. Chen, Opt. Lett. **39**, 6339 (2014).

[20] D. Budker and D. F. J. Kimball, *Optical Magnetometry* (Cambridge University Press, Cambridge, 2013).

[21] G. A. Smith, A. Silberfarb, I. H. Deutsch, and P. S. Jessen, Phys. Rev. Lett. **97**, 180403 (2006).

[22] C. A. Riofrío, P. S. Jessen, and I. H. Deutsch, J. Phys. B **44**, 154007 (2011).

[23] K. Hammerer, A. S. Sørensen, and E. S. Polzik, Rev. Mod. Phys. **82**, 1041 (2010).

[24] A. Kuzmich, L. Mandel, and N. P. Bigelow, Phys. Rev. Lett. **85**, 1594 (2000).

[25] E. E. Mikhailov and I. Novikova, Opt. Lett. **33**, 1213 (2008).

[26] B. Julsgaard, A. Kozhekin, and E. S. Polzik, Nature (London) **413**, 400 (2001).

[27] B. Julsgaard, J. Sherson, J. I. Cirac, J. Fiurášek, and E. S. Polzik, Nature (London) **432**, 482 (2004).

[28] J. F. Sherson, H. Krauter, R. K. Olsson, B. Julsgaard, K. Hammerer, I. Cirac, and E. S. Polzik, Nature (London) **443**, 557 (2006).

[29] M. W. Sørensen and A. S. Sørensen, Phys. Rev. A **77**, 013826 (2008).

[30] B. Q. Baragiola, L. M. Norris, E. Montaño, P. G. Mickelson, P. S. Jessen, and I. H. Deutsch, Phys. Rev. A **89**, 033850 (2014).

[31] G. Vasilakis, V. Shah, and M. V. Romalis, Phys. Rev. Lett. **106**, 143601 (2011).

[32] G. A. Smith, S. Chaudhury, A. Silberfarb, I. H. Deutsch, and P. S. Jessen, Phys. Rev. Lett. **93**, 163602 (2004).

[33] G. A. Smith, S. Chaudhury, and P. S. Jessen, J. Opt. B **5**, 323 (2003).

[34] D. V. Vasilyev, K. Hammerer, N. Korolev, and A. S. Srensen, J. Phys. B **45**, 124007 (2012).

[35] E. Montano, Ph.D. thesis, University of Arizona, 2015 .

[36] G. Lamporesi, J. Catani, G. Barontini, Y. Nishida, M. Inguscio, and F. Minardi, Phys. Rev. Lett. **104**, 153202 (2010); R. H. Leonard, A. J. Fallon, C. A. Sackett, and M. S. Safronova, Phys. Rev. A **92**, 052501 (2015); **95**, 059901(E) (2017).

[37] L. J. LeBlanc and J. H. Thywissen, Phys. Rev. A **75**, 053612 (2007).

[38] J. M. Geremia, J. K. Stockton, and H. Mabuchi, Phys. Rev. A **73**, 042112 (2006).

[39] J. K. Stockton, Ph.D. thesis, California Institute of Technology, 2007 .

[40] I. H. Deutsch and P. S. Jessen, Phys. Rev. A **57**, 1972 (1998).

[41] W. F. Holmgren, R. Trubko, I. Hromada, and A. D. Cronin, Phys. Rev. Lett. **109**, 243004 (2012).

[42] B. Arora, M. S. Safronova, and C. W. Clark, Phys. Rev. A **84**, 043401 (2011).

[43] Typically, this result is simplified by taking $\lambda \approx \lambda_{J'}$.

[44] I. H. Deutsch and P. S. Jessen, Opt. Commun. **283**, 681 (2010).

[45] M. Koschorreck, M. Napolitano, B. Dubost, and M. W. Mitchell, Phys. Rev. Lett. **105**, 093602 (2010).

[46] A. A. Wood, L. M. Bennie, A. Duong, M. Jasperse, L. D. Turner, and R. P. Anderson, Phys. Rev. A **92**, 053604 (2015).

[47] Y.-J. Lin, A. R. Perry, R. L. Compton, I. B. Spielman, and J. V. Porto, Phys. Rev. A **79**, 063631 (2009).

[48] A. A. Wood, L. D. Turner, and R. P. Anderson, Phys. Rev. A **94**, 052503 (2016).

[49] J. Söding, D. Guéry-Odelin, P. Desbiolles, F. Chevy, H. Inamori, and J. Dalibard, Appl. Phys. B **69**, 257 (1999).

[50] P. C. D. Hobbs, Appl. Opt. **36**, 903 (1997).

[51] The Nyquist frequency is therefore 1 MHz, limiting the maximum Larmor frequency and thus magnetic field strength to 1.4 G without undersampling. We have subsequently incorporated an AlazarTech ATS9462 ditigizer (16-bit, 180 MS/s) to acquire Faraday signals at higher magnetic fields.

[52] W. Zhang, D. L. Zhou, M.-S. Chang, M. S. Chapman, and L. You, Phys. Rev. A **72**, 013602 (2005).

[53] If the spectrogram resolution is much finer than the quadratic splitting, $\Delta f < q_{\rm net}/2\pi$, the amplitude modulation is instead resolved as two sidebands at $f_\pm = f_L \pm q_{\rm net}/2\pi$.

[54] F. Gerbier, A. Widera, S. Fölling, O. Mandel, and I. Bloch, Phys. Rev. A **73**, 041602 (2006).

[55] Note that imperfect linear polarization of the microwave source causes a correction to the induced quadratic shift from the other Zeeman substates.

[56] G. Breit and I. I. Rabi, Phys. Rev. **38**, 2082 (1931).
[57] We average the shot noise over a 20 ms interval prior to tipping the spins across a 2 kHz frequency band around the mean Larmor frequency.
[58] M. V. Romalis, in *Optical Magnetometry*, edited by D. Budker and D. F. J. Kimball (Cambridge University Press, Cambridge, 2013), pp. 25–39.
[59] M. J. Martin, Ph.D. thesis, University of Colorado, 2013.